Research article

Junhu Zhou[a], Chenxi Zhang[a], Qirui Liu, Jie You, Xin Zheng, Xiang'ai Cheng and Tian Jiang*

Controllable all-optical modulation speed in hybrid silicon-germanium devices utilizing the electromagnetically induced transparency effect

Abstract: Incorporating auxiliary all-optical modulation speeds as optional response modes into a single metamaterial is a promising research route towards advanced terahertz (THz) applications ranging from spectroscopy and sensing to communications. Particularly, a plethora of dynamically tunable optical functionalities are determined by the resonant light-matter interactions. Here, an electromagnetically induced transparency (EIT) resonator stacked with two traditional semiconductor films, namely silicon (Si) and germanium (Ge), is experimentally demonstrated. A giant switching feature of the EIT window with a peak at 0.65 THz occurs when the Si or Ge film is excited by ultrafast optical pulses, allowing for an optically tunable group delay of the THz wave packet. The recovery time for the slow and fast on-off-on switching cycles is 1.7 ns and 11 ps, respectively, which are mapped as the pump delay time of Si and Ge. Two optional response modes are integrated on the same device, where the modulation speed varies by three orders of magnitude, endowing the modulator more compact. This work provides new prospects for the design and construction of novel chip-scale THz devices based on EIT and their applications in areas of sophisticated optical buffering and active filtering.

1 Introduction

The recent metamaterial advancements have inspired the exploration of many extraordinary phenomena, including the negative refractive index [1, 2], sensing [3], electromagnetic cloaking [4, 5], perfect absorber [6, 7], and superlenses [8]. Precisely, metamaterials are artificial designed periodic structure arrays that exhibit great flexibility in custom-built functionalities, which are determined by size, shape, and arrangement. Electromagnetically induced transparency (EIT) is a destructive interference effect that occurs in a three-level atomic system, which gives rise to a sharp transparency window in a broad electromagnetic wave spectrum. Importantly, this effect can be utilized to engineer the dispersive properties of an initially opaque media on a large scale, making possible for the appearance of slow light phenomena [9–11]. Metamaterial structures with effective medium characteristics, such as cut wires (CWs) and split-ring resonators (SRRs), make the realization of bulk EIT analogues promising due to Fano-type linear destructive interference [11–13], without the scathing experimental requirements of optical implementations [14–16].

Fano resonance possesses high sensitivity to the local electromagnetic environment of the resonator [17]. And rapid strides have been devoted to the dynamic tuning of metamaterials by external stimuli such as heat [18], light [19–21], or voltage bias [22, 23]. Among those options, all-optical modulation is of preference, due to their ultrafast optically tunable permittivity and advantage of integration

[a]**Junhu Zhou and Chenxi Zhang:** These authors contributed equally to this work.
***Corresponding author: Tian Jiang,** College of Advanced Interdisciplinary Studies, National University of Defence Technology, Changsha, 410073 Hunan, China, e-mail: tjiang@nudt.edu.cn. https://orcid.org/0000-0003-3343-5548
Junhu Zhou and Xiang'ai Cheng: College of Advanced Interdisciplinary Studies, National University of Defence Technology, Changsha, 410073 Hunan, China; State Key Laboratory of Pulsed Power Laser Technology, Changsha, 410073 Hunan, China; and Hunan Provincial Key Laboratory of High Energy Laser Technology, Changsha, 410073 Hunan, China
Chenxi Zhang and Qirui Liu: College of Advanced Interdisciplinary Studies, National University of Defence Technology, Changsha, 410073 Hunan, China
Jie You and Xin Zheng: National Innovation Institute of Defence Technology, Beijing 100010, P.R. China

with present microelectronic and optoelectronic device technology platforms [24–30]. In the past, traditional photosensitive semiconductors, silicon (Si) and gallium arsenide (GaAs), have been widely exploited in a variety of photonic metamaterial devices [31–36]. Placing Si or GaAs islands in the split gap strategically provided a valuable insight into optical tuning terahertz (THz) metamaterials. More recently, transition metal dichalcogenide (TMDC) film [19, 37] and solution-processed perovskite thin film [38–40]–based active devices have been demonstrated at THz frequencies with numerous desired features such as ultrasensitive or ultrafast response. The ultrafast recovery time of the photoactive switching is a significant indicator for an all-optical system in the field of advanced photonics [41–48]. Equally important, the slow speed response and the broadened time window make the device more tolerate to the uncertainty of the delay time of external stimuli. Based on the point of enriching multifunctional THz devices, discretionary dynamic response modes should be incorporated for a wider range of applications. Unprecedented merits in terms of the simplification and cost are offered by the economical and an extremely easy process of integrating the spin-coated perovskite film or chemical vapor deposition–grown large-area TMDC film on top of the metamaterial surface [37–40]. Inspired by this, we demonstrate an active and speed-selectable EIT metamaterial using layer stacked commercial Si-on-sapphire (SoS) substrate and germanium (Ge) film.

Similar to Si, Ge is an indirect bandgap semiconductor, whose fundamental energy bandgap is 0.66 eV (0.14 eV lower than the direct bandgap), and also exhibits great potential for dynamic modulation. Compared with Si, Ge possesses a larger intrinsic carrier concentration and a higher carrier mobility [49, 50] as well as good compatibility with complementary metal-oxide-semiconductor foundries. In our device layout, Ge is simply evaporated as single layer over the Fano-resonant metamaterial array on the epitaxially grown SoS substrate. Different from the ErAs/GaAs superlattices where ultrafast photoswitching of inductive-capacitive (LC) resonances were achieved previously [51], amorphous Ge has structural defects that result in trap-assisted recombination sites [49, 52], which helps promote ultrafast carrier recombination (around three orders of magnitude faster than superlattices) and the device fabrication based on it requires no alternating between materials. This is because it only involves the deposition of a single-element semiconductor film, instead of satisfying the lattice matching condition. Meanwhile, there is no strict alignment requirement for this two-step photolithography in the semiconductor-island-integrated metamaterial unit cells [53, 54]. As a consequence, this fabrication process is found to be convenient, efficient, and economical.

In this article, we present a comprehensive investigation on the THz transmission modulation and the optical reconfiguration of EIT metamaterial structure which is based on different electromagnetic environments by hybridizing Ge and Si films as active mediums with an Au EIT array. From the transient transmission using the optical-pump-THz-probe (OPTP) system, we find that the ultrafast dynamic behavior within the picosecond of all-optical modulation in the amorphous Ge, together with the slow speed response defined by the integrated Si film, makes the device more tolerable to the uncertainty of delay time. Such device highlights the potential of controllable all-optical modulation speed and the simple fabrication steps based on Ge and SoS substrate. Furthermore, this optically tunable EIT metamaterial may also inspire research interest in the development of electrically and mechanically tunable THz devices with novel functionalities and compact footprints.

2 Results and discussion

2.1 Sample preparation and characterization

The schematic architecture of the EIT THz device with a controllable modulation speed is depicted in Figure 1A, where the proposed device owns a stacked structure that is composed of four layers of functional materials, namely a sapphire substrate, a Si film, a metal resonance pattern, and a Ge film. The metal structure acts as the initial resonator, who generates the EIT resonance within the designed frequency range. The Si and Ge films serve as the photon-active media with a slow recovery speed and a fast recovery speed, respectively. This enables the dielectric environment on the surface of the metal resonator to be controlled by pump beam and leads to an active modulation effect on the EIT resonance window. Owing to the material difference between the front and back surfaces of the resonators, the modulator is designed to present diverse modulation speeds when a pump pulse separately irradiates the Si and Ge film. The fabrication processes starts with a commercially available SoS wafer comprising a 500-nm-thick intrinsic epitaxial Si layer formed on 500-μm-thick R-plane sapphire substrate. The periodic array of CWs and the SRR pair patterns is first fabricated by using the conventional photolithography technique, where the 190-nm-thick gold (Au) structures is deposited on SoS substrate by E-beam evaporation and then
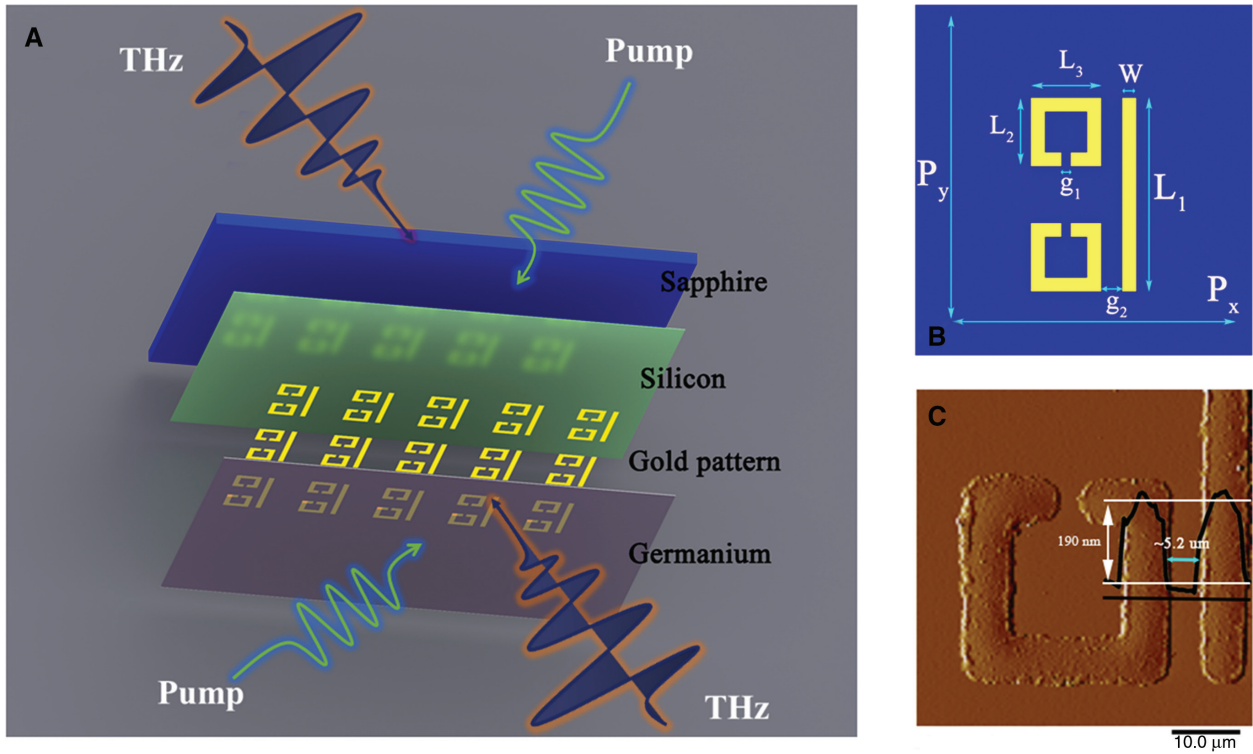
Figure 1: Characterization and schematic diagram of the modulation-speed controllable THz device.
(A) Principle schematic diagram of the proposed metamaterial integrated with a layer of Si (500 nm) and Ge film (600 nm) on the lower and upper surfaces of the gold resonators, whose response speed is tunable. The Si and Ge films can be excited by forward and backward optical pump pulses as a photoactive layer. (B) Schematic view of the functional unit cell. The geometrical parameters are as follows: $L_1 = 85$ μm, $L_2 = L_3 = 30$ μm, W = 6 μm, $g_1 = 4$ μm, $g_2 = 5$ μm. The period is $P_x = 80$ μm, $P_y = 120$ μm. The height of the Au pattern is 190 nm. (C) Atomic force microscope (AFM) image of one corner of a unit cell. Inset: the AFM line scan corresponding to the gap of g_2. Scale bar, 10 μm.

the patterned photoresist layer is lifted off subsequently, thereby leaving the desired Au EIT resonator array on substrate. Finally, a 600-nm-thick film of noncrystalline Ge is thermally evaporated onto the planar gold array. It is noticeable that Au has an excellent chemical stability and an ultrahigh conductivity ($>4.56 \times 10^7$ S/m), serving as a perfect electrical conductor in THz metasurface. The size of the fabricated sample is 4×4 mm².

The detailed geometrical parameters of an individual unit cell are presented in Figure 1B. Specifically, a pair of SRRs with the same size are aligned face to face in the vertical direction, and the arm length in horizontal and vertical directions is $L_3 = L_2 = 30$ μm. The premeditated distance of the split gap is g_1 μm. A CW resonator with a length of $L_1 = 85$ μm is displaced on the right of SRR pairs. The resonance frequency of the dark mode is determined by the split gap g_1 and arm length L_3 of the SRRs, while the resonance frequency of the light mode is determined by the length L_1 of the CW resonator. The separation length in the middle of the CRRs and CW is set to be $g_2 = 5$ μm to ensure enough coupling strength between each other. Additionally, the metamaterial unit cell is also characterized by

atomic force microscopy, as shown in Figure 1C, where the uniform surface morphology is observed, ensuring the good film coverage and metal structural integrity of THz dynamic modulator.

Optical property characterization of the hybrid metamaterial modulator is performed by a high-performance OPTP system (TTT-02-OPTP, TuoTuo Technology). The nonlinear THz generation and electro-optic detection are based on two 1-mm-thick ZnTe crystals. A light source of 1 kHz repetition optical pulses of 800 nm (center wavelength) with a pulse width of 100 fs (full width at half maximum) is split for optical pumping of the Si and Ge film, respectively. Focused THz beam (~2.2 mm diameter) is collimated on the Au array with electric field parallel to the CW. The spatially overlapping pump spot with a 5-mm-diameter enables a uniform excitation aperture for the THz transmission. The THz time-domain waveforms are collected by moving the step stage of the gating pulses within certain pump fluences and pump delay time. To obtain the frequency-dependent THz amplitude E(ω), the time-domain waveforms is converted into the frequency-domain by standard Fourier transformation. For easy

analysis, the transmission spectra of the sample $E_s(\omega)$ are normalized to the transmission spectra of air $E_{air}(\omega)$, following the relation of $|T(\omega)| = |E_s(\omega)/E_{air}(\omega)|$. By gradually changing the pump delay and recording the THz time-domain waveforms, the transient evolution process of the photo-switching cycle in EIT resonance can be mapped.

The all-optical modulation of hybrid EIT metamaterial transmission resonance is elegantly repeated in numerical simulations conducted by the commonly used finite element method. In this electromagnetic simulation model, the permittivity of the sapphire substrate is selected to be 11.5 according to the extracted result of THz time domain spectroscopy test. Si and Ge are ascribed to have fixed real relative permittivities of 11.7 and 16 with intrinsic conductivity $\sigma = 0.01$ S$\star$m^{-1}. The normal incident THz plane wave is taken to propagate in the z-direction, with the polarization of electric field parallel to the CW. Periodic boundary condition is utilized to describe the continuous Au array. Photoexcited carrier density $\Delta N_{e\text{-}h}$ of Si and Ge is used to calculate the frequency-dependent complex conductivities according to the Drude model. The time-dependent $\Delta N_{e\text{-}h}$ is obtained by the fitting the result of carrier relaxation equation with the maximum charge carrier concentration determined by matching the experimental results.

2.2 Dynamic control of the EIT resonance

To explain the underlying mechanism of the EIT effect, we simulated the amplitude transmission spectra of SRR pair and CW separately without excitation. In the CW array, a typical localized surface plasmon (LSP) resonance of electric dipole can be strongly excited by the incident light, which exhibits a broad dip at 0.71 THz in the transmission spectra of Figure 2A. As for the SRR-pair array, since the electric field is parallel to the capacitor (split gap) of SRRs, it cannot couple to the resonator [55]. Meanwhile, there is also no magnetic resonance because the magnetic field is completely parallel to its plane. As a consequence, the inductive-capacitive (LC) resonance of the SRR-pair array is suppressed, showing no dip in the transmission spectra in Figure 2A. However, according to the induction law, the circulating surface current with the magnetic-dipole moment normal to the SRR plane can be induced by the magnetic field with component normal to the plane, operating as a dark resonator that couples indirectly to the incident light. When CW is introduced in the EIT metamaterial sample, the circulating current in the SRR can be initiated via the Fano-type near-field coupling [12]. A narrow transparent window near 0.63 THz occurs within the broad dipole resonance dip background, due to the destructive interference between the direct excitation pathway of electric dipole resonance and the indirect excitation pathway of magnetic dipole resonance. The electric field distribution corresponding to the transparency peak with the high electric field localized at the split gap of SRRs is shown in Figure 4A and B.

Optical pump fluence is regarded as a key parameter employed to tuning the resonance intensity in a metasurface. Figure 3 shows the spectral dispersion of transmission at the pump delay time with a maximum modulation
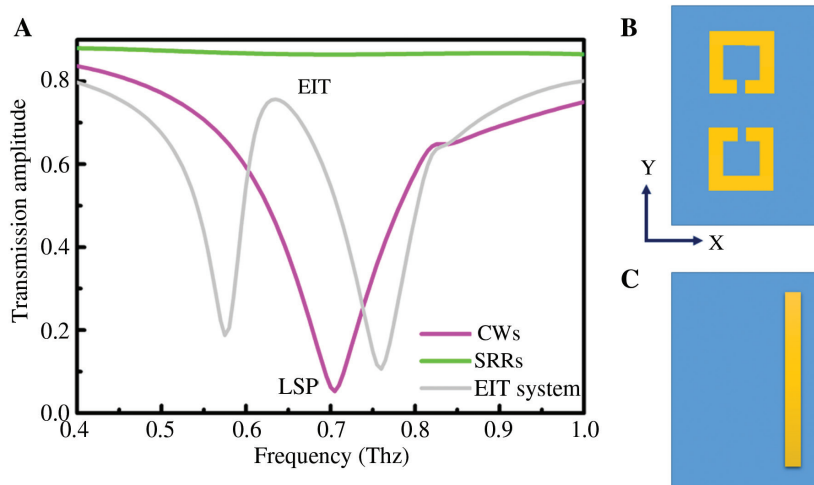

Figure 2: Simulated transmission spectra without excitation.
(A) Simulated amplitude transmission property of the sole CWs, SRRs, and the EIT metamaterial sample. (B) and (C) are the structural geometries of the SRRs pair and CW, respectively. Corresponding to the illustration, the incident THz electric fields is polarized in the Y direction.
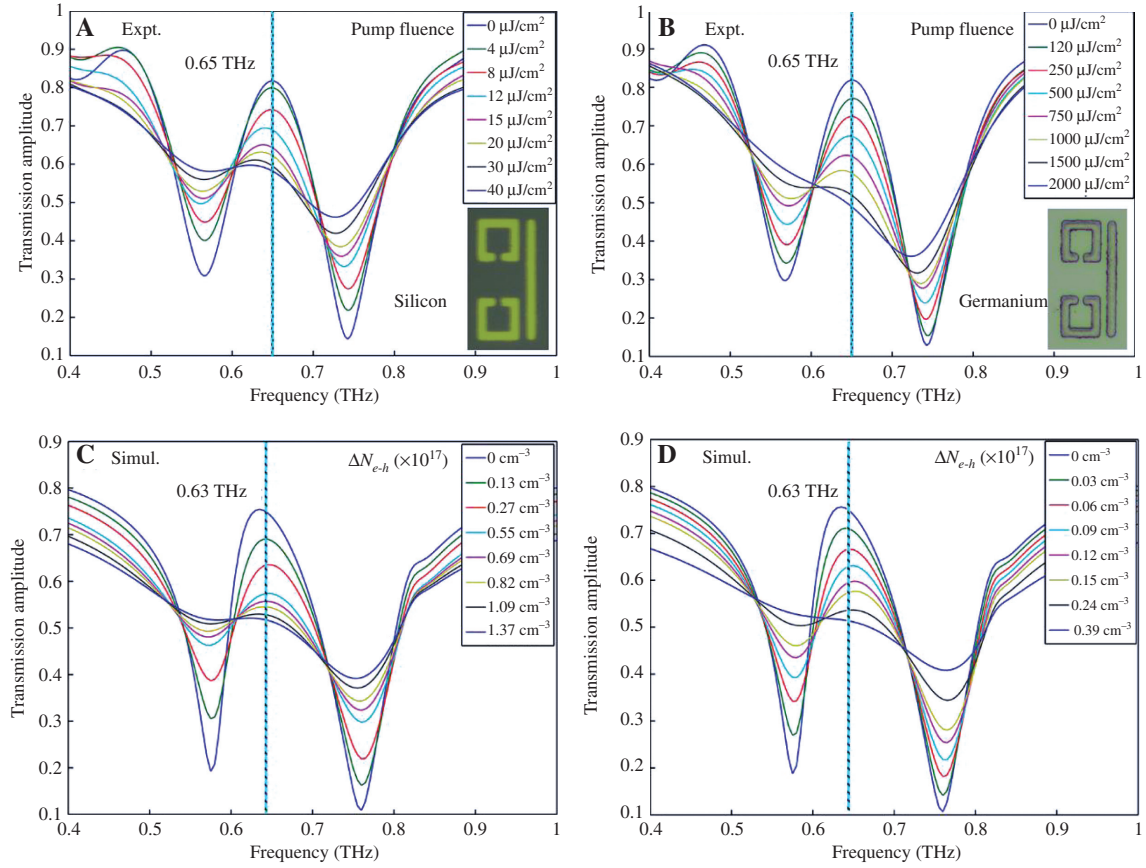
Figure 3: Normalized results of the all-optical modulation in amplitude transmissions spectra.
Optically pump-power-controlled active tuning of the transmitted amplitude of EIT window at 0.65 THz is achieved by changing the photoconductivity of (A) Si and (B) Ge films. The corresponding numerically simulated transmission results are shown in (C) and (D), respectively, as a function of photoexcited carrier density $\Delta N_{e\text{-}h}$. The insets in (B) and (A) are the microscopic images of the front and back surfaces of a unit fabricated metamaterial on the sapphire substrate. The dashed line represents the EIT frequency of resonance system.

depth. A strong EIT resonance feature is observed in the experimentally measured transmission spectrum of THz electric field amplitude. In Figure 3A and B, the EIT window is located at the frequency of 0.65 THz. In the case where the pump fluence is blocked, the hybrid metamaterial device maintains a normalized amplitude transmittance of 83% at the position of the resonance peak, despite the influence imposed by the intrinsic conductivity of the Si and Ge films. With the increasing optical pump fluence, the EIT resonance, which is characterized by a transmission peak at 0.65 THz and dip at 0.57 THz, is increasingly suppressed as the density of electrons transition into the conduction band increases. Due to the large discrimination in photon-photoconductivity ($\Delta\sigma$) conversion efficiency between Si and Ge, the pump fluences used for photon doping are different. A series of the pump fluences ranging from 4 to 40 μJ/cm² for Si and 120 to 2000 μJ/cm² for Ge are employed in this work. Under the maximum pump fluence, the transmission ratio at the

transparency window dropped to 0.58 (Si) and 0.49 (Ge), and the trend towards saturation is clearly visualized with the EIT peak almost completely vanishing. At this point, the difference between transmission levels at the peak and dip of the EIT resonance is reduced to ≈3% (Si) and −10% (Ge) (normalized to the magnitude in the absence of pump pulses), where the negative result suggests that the EIT resonance has completely disappeared.

The experimental result is well reproduced by the numerical simulation using the finite element method. Limited by the accuracy of the photolithography process, the geometric parameters of the Au structure might slightly deviate from the original design and cause the EIT window to drift 0.02 THz. As described by Figure 3C and D, the transmission property is viewed as a function of photoexcited carrier density $\Delta N_{e\text{-}h}$. By matching the simulation and measured results, $\Delta N_{e\text{-}h}$ is optimized to a proper value, which is then considered as the initial injection condition of nonequilibrium carriers

for the next simulation process. For the pump fluence of 40 μJ/cm² and 2000 μJ/cm² in Figure 3A and B, the corresponding ΔN_{e-h} values are 1.37 and 0.39×10^{17} cm⁻³, respectively. Next, the frequency-resolved conductivities of the doped Si and Ge films are calculated by the Drude model [56]:

$$\sigma(\omega) = \frac{e^2 N_{e-h}}{m^*} \times \frac{i}{\omega + i\tau_d} \tag{1}$$

where e is the electronic charge (1.602×10^{-19} C), N_{e-h} is the charge carrier density, and m^* is the optical effective mass of the charge carriers. For Si and Ge, m^* are 0.07 m_0 and 0.15 m_0, respectively. τ_d is the scattering time, which is defined as the average time between consecutive scattering events. In this context, τ_d is assumed to be 35 fs for Si [50] and 70 fs for Ge [57]. The saturation tendency of modulation effect to photon doping is also revealed by ΔN_{e-h}. At a low charge carrier density, the EIT window is more sensitive to the change of ΔN_{e-h}, whereas the maximum pump fluence we used here has brought the device nearly saturated.

To explore the underlying physics of the active EIT behavior, the widely used coupled Lorentz oscillator model is adapted to analyze the near field Fano-type interaction between the two bright and dark modes in the EIT metamaterial unit cell [14]:

$$\begin{pmatrix} \omega_1 - \omega - i\gamma_1 & \kappa \\ \kappa & \omega_2 - \omega - i\gamma_2 \end{pmatrix} \begin{pmatrix} x_1 \\ x_2 \end{pmatrix} = i \begin{pmatrix} f_1 \\ f_2 \end{pmatrix} \tag{2}$$

Here, x_1 and x_2 are the oscillator amplitudes, ω_1 and ω_2 are the resonant frequencies, γ_1 and γ_2 are the damping coefficients, and f_1 and f_2 are the external forces with the driving frequency ω. The coupling constant κ describes the interaction between the oscillators.

The small photoexcited carrier density ΔN_{e-h} is not sufficient to induce a significant shift of the resonance frequencies for both bright and dark modes, so the EIT frequency still remains near 0.63 THz with a subtle change when excited by different pump fluences, as depicted in Figure 3C and D. However, the damping of dark mode γ_2 becomes much stronger, because the current flow is impeded by the increasing ohmic losses in the Si or Ge film due to the photoexcited carrier. In the meantime, the effective length of these two resonant elements turns larger as the conductivity σ_{Si} or σ_{Ge} increases, leaving the coupling coefficient κ between the two modes smaller. Hence, the coupling effect between bright and dark modes becomes much weaker, which causes a dramatic decrease in the electric field localized at the split gap of SRRs, as
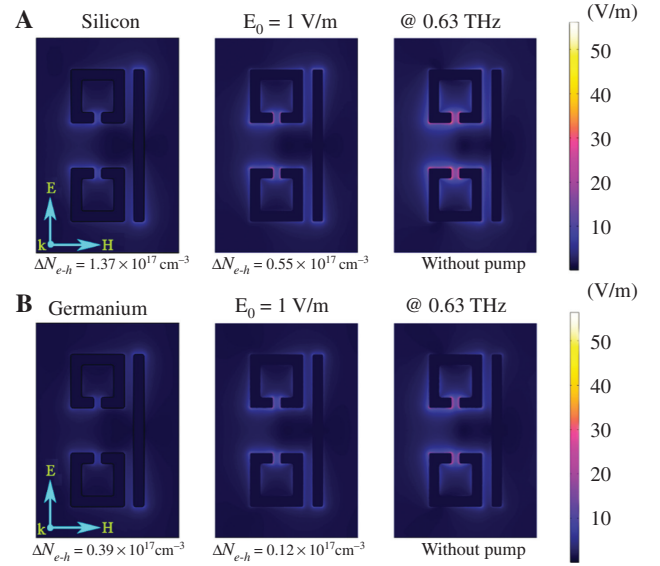

Figure 4: Calculated electric field distributions in the transverse plane of the EIT Au metasurface at 0.63 THz.
(A) Simulated evolution of electric field distributions vs. the charge carrier density ΔN_{e-h} from 0 to 0.55 and 1.37×10^{17} cm⁻³ of the Si film. (B) The evolution of electric field distributions vs. the carrier density ΔN_{e-h} from 0 to 0.12 and 0.39×10^{17} cm⁻³ of the Ge film. Incident fields are normalized as $E_0 = 1$ V/m. Polarization directions of electric field of incident fields are marked by the white arrow.

displayed in Figure 4A and B. Subsequently, it can be seen from Figure 3C and D that the EIT-like resonance strength weakened as the photoexcited carrier density ΔN_{e-h} increases from 0 to 1.73 and 0.39×10^{17} cm⁻³, respectively. In the meantime, the transparency windows broaden non-negligibly with slight shifts of the resonance frequencies.

Figure 5A and B show the time-resolved THz transmission of the Si and Ge films in the absence of artificial structure. Rather than strategically place the Si or Ge islands in the gap of the metal resonators, the measured device is uniformly covered by the Si and Ge films. After the photon injection process, the semiconductor thin films would lead to a modulation of the entire part excited by laser, including the EIT resonance regions as well as the nonresonant regions. Unlike the EIT resonance, which is more susceptible to interface environment, the light-induced change of photon-media films are relatively small, as shown in Figure 5. The transient negative differential transmission $-\Delta T/T$ is proportional to $\Delta\sigma$, and consequently, these curves directly describe the photo-conductivity of the film vs. pump delay time. Si and Ge are both indirect band-gap semiconductors whose photoluminescence yield of electron-hole pair recombination can be negligible. Therefore, it is concluded that the recombination processes of these two materials are mainly
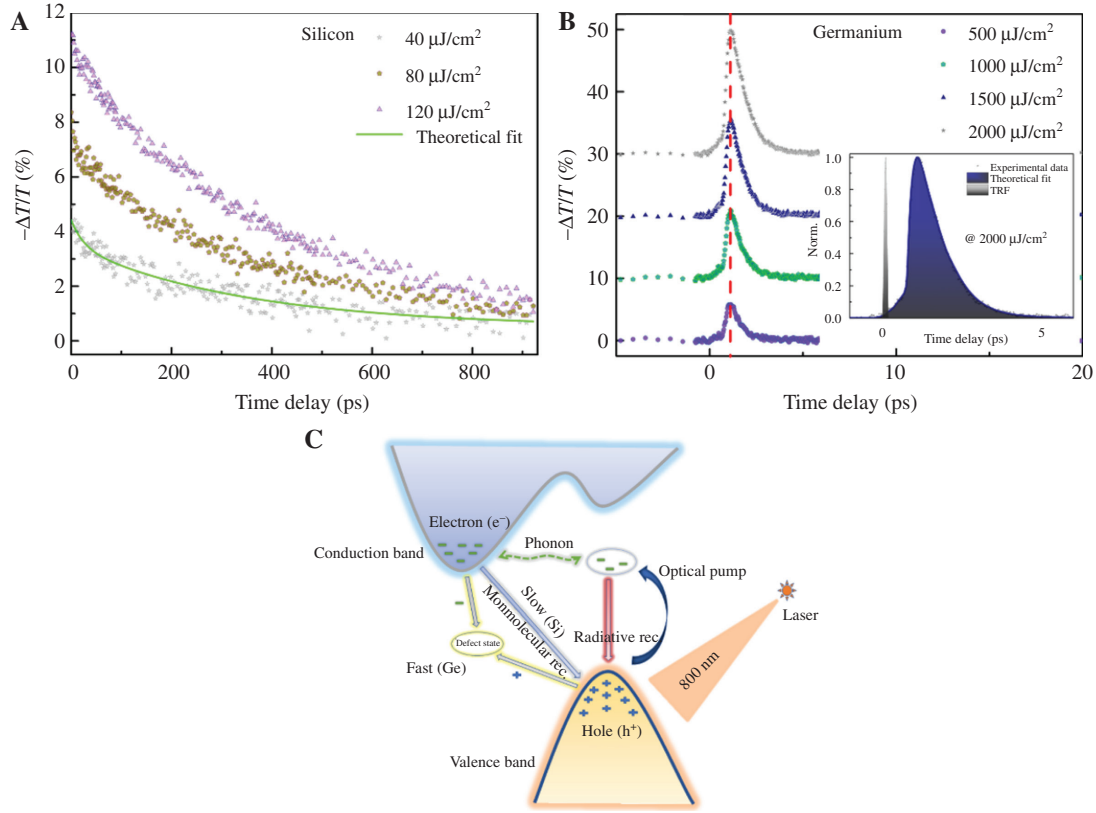
Figure 5: Measured transient negative differential transmission $-\Delta T/T$ for Si and Ge thin films implemented by using OPTP measurements for various pump fluences.
The solid curves represent the fittings of recombination processes by utilizing rate equations, whereas the dotted lines are measured by experiment. (A) Normalized and time-resolved THz transmission curve of Si film under the pump fluences of 40, 80, and 120 μJ/m². (B) Normalized and time-resolved THz transmission curve of Ge film under the pump fluences of 500, 1000, 1500, and 2000 μJ/m². Plots are shown with vertically offset for clarity. The inset presents the fit result and corresponding instrument response function. (C) Diagrammatic sketch of photoexcited carrier transitions in Si and Ge films.

dominated by the monomolecular recombination. The difference is that a large amount of defect states are induced by the Ge film during the thermal evaporation fabrication. As photoexcited carriers relax from the conduction to the valence band, defect states present within the band act as trap-assisted recombination sites in the noncrystalline Ge where the carrier recombination is greatly boosted. Figure 5C presents a concise explanation for the relaxation dynamics of the nonequilibrium carriers in Si and Ge.

To accurately characterize the temporal evolution processes, a single exponential decay equation is exploited to fit the experimental results,

$$-\frac{\Delta T}{T}(t) = Ae^{-\frac{t}{t_1}} \tag{3}$$

The best-fitting result of Si is plotted in Figure 5A as a solid line with a decay time constant $t_1 = 442$ ps. In the case of Ge film, the entire process completes just within

several picoseconds. Consequently, we must consider that the experimental data is the convolution of the real signal and the instrument response function (IRF).

$$-\frac{\Delta T}{T}(t) = \mathrm{IRF} \otimes Ae^{-\frac{t}{t_1}} \tag{4}$$

The IRF and fitting results are illustrated in the inset, with the decay time extracted to be $t_1 = 0.65$ ps. This is an impressively short characteristic time, which is three orders of magnitude smaller compared to Si materials. The huge difference between time constants makes it possible to integrate two selectable response speeds in a single modulator, which is expected to simultaneously possess an ultrafast switching and a slower option for the purpose of providing a sufficiently long modulation window. Based on the accurate mathematical description of the dynamic curve and the predefined initial injection value of nonequilibrium carriers (the pump fluence of 40 μJ/cm²

for Si and 2000 µJ/cm² for Ge), we have investigated the evolution of the time-resolved EIT resonance to verify the proposed slow and fast process in numerical calculation.

Our key results of the transient evolution process are presented in Figures 6 and 7. From these two figures, one can clearly observe a slow and a fast photo-switching cycle in false color images without crosstalk between each other. The penetration depth of the 800 nm laser in Si and Ge materials are 1176 and 203 nm [49, 58], respectively. A 600-nm Ge film is sufficient to absorb all incident light, but the epitaxial Si film cannot block the pump pulses totally. However, considering that the pump fluences used to achieve the similar modulation depth is 50 times different between Si and Ge, the leakage from the Si film can be ignored for the Ge film. Specifically, even excluding the attenuation due to reflections and aborption, the maximum pump fluence of 40 µJ/cm² (the EIT resonance has almost disappeared) is only equivalent to one third of the minimum power applied to Ge film.

Therefore, the experimental result shown in Figure 6A is a purely a slow cycle with no participation of fast process. Here, the time delay represents the mismatch between the arrival of the excitation and the THz probe at the sample position. As illustrated in Figure 6, limited by the length of the optical delay line used in the experiment, the maximum time delay can only be extended to 900 ps, which is too short to cover an intact switching cycle for the slow change evolution process. Thus, the completed progress is supplemented by simulation. As the pump pulse impinges on the Si film, a large density of electrons is injected into the conductive band. Due to the quasi-metal transition of Si, the capacitive gaps of the SRRs are short-circuited and the screening effect of the fringing field by the Si film is significantly strengthened, which leads to the deterioration of the dark mode as well as the destructive interference between the LC and LSP resonance. Thereby, a strong modulation is imposed at the delay time around 0 ps, as exhibited by Figure 6. Distinct
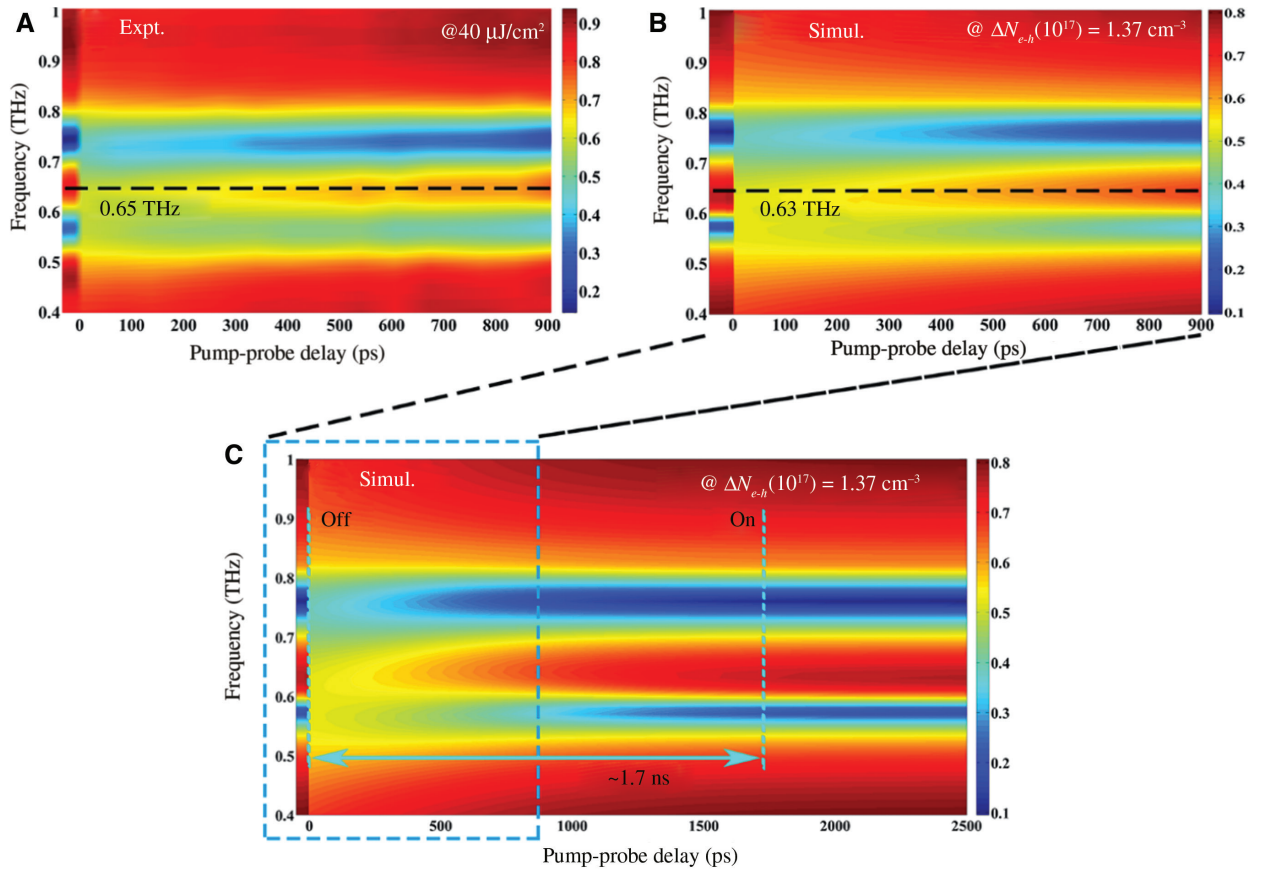

Figure 6: Transient evolution process of the slow switching changes in EIT resonance with the Si film is activated.
(A) Experimental transmission spectra map of the hybrid photonic device vs. the pump-probe time delay. The pump fluence is 40 µJ/cm².
(B) Simulation results of the first 900 ns of the transmission spectra map. (C) Simulation results of the entire photo-switching cycle of the active EIT resonance device in slow recovery speed. The recombination rate equation of the nonequilibrium carriers ($\Delta N_{e\text{-}h}$) obtained from the fitting result is used in numerical calculation by assuming the maximum $\Delta N_{e\text{-}h}$ is 1.37×10^{17} cm⁻³.

to the dipole resonance, the EIT resonance is more susceptible to dielectric changes around its surface environment; thus, its temporal evolution resonance recovers more slowly, as depicted in Figure 6C. Particularly, the EIT resonance is still moderately affected by the photoconductivities until a time delay of 1.7 ns. After this, relaxation of the carriers eventually restores the original spectral property within 1.7 ns.

The experimental and simulation results of the fast switching circle in the Ge film are shown in Figure 7. The basic evolution of Ge is similar to that of Si, but its relaxation characteristic time is only 0.65 ps, which is almost comparable to the photon injection process, allowing for the total on-off-on circle accomplished within 11 ps (90 GHz). In the meantime, the modulation window is seriously compressed in which the transmission spectrum changed drastically in a very short time, so the delay time

needs to be controlled precisely (sub-picosecond scale) in the modulation practice. In contrast, as displayed in Figure 6A, the transmission spectrum of slow cycle switching that lasts more than 900 ps changes gently and uniformly, resulting in a more accurate modulation output under the same delay time definition.

In order to eliminate the fake EIT effect that may be concealed in the transmission amplitude, the optically tunable active group delay (Δt_g) of the THz wave packet is retrieved from the measured complex transmissions as the derivative of phase with respect to circular frequency at various photoexcitations. It can been seen from Figure 8 that the wave packet with a central frequency of 0.65 THz is delayed by 1.9 ps without pump excitation and the delay time decreases as the pump increases, reaching almost zero at the pump maximum. Therefore, we can conclude from Figure 8 that the slow light characteristic of
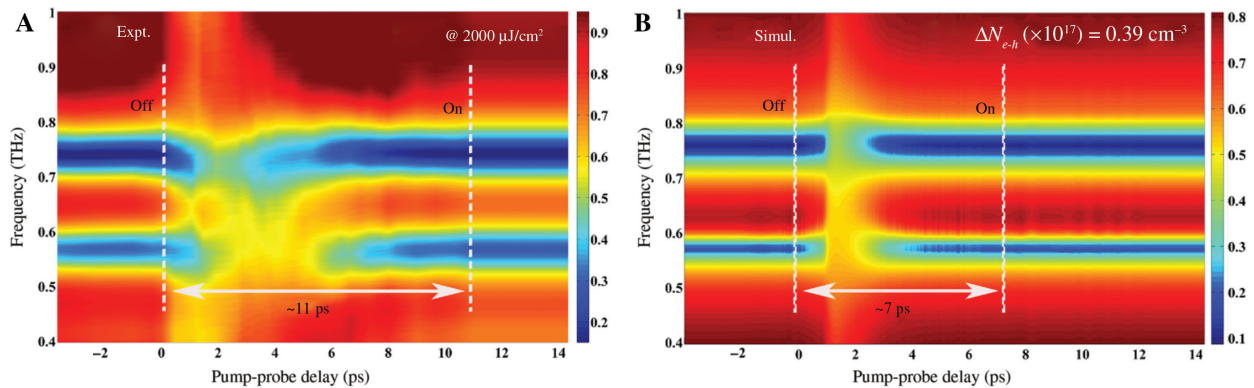

Figure 7: Transient evolution process of the fast switching changes in EIT resonance with the Ge film is activated.
(A) Measured transmission spectra map of the hybrid photonic device vs. the pump-probe time delay. The entire photo-switching cycle of the active EIT resonance device in fast recovery speed is presented. The pump fluence is 2000 µJ/cm². (B) The corresponding simulated result of the optical modulation process. The measured recombination curve of the nonequilibrium carriers ($\Delta N_{e\text{-}h}$) is used in numerical calculation by assuming the maximum $\Delta N_{e\text{-}h}$ is 0.39×10^{17} cm⁻³.
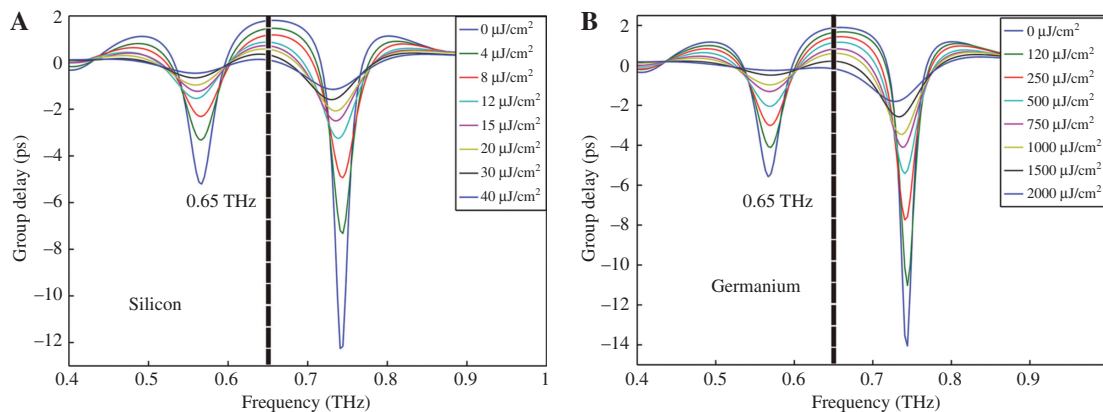

Figure 8: Optically tunable active group delay data extracted from experiment results as a function of pump fluence.
(A) The pump pulses are back-propagated and the Si film is photon doped. (B) The pump pulses are travel forward and the Ge film is excited.

EIT resonator gradually disappears as the pump fluences increases, and eventually vanishes.

3 Conclusion

In summary, we have experimentally and numerically established a novel planar metamaterial device comprising an Au EIT array hybridized with Ge and Si films as active media, which is confirmed to have the speed-selectable optical reconfiguration and THz transmission modulation characteristics. Our comprehensive results suggest that the resonant THz transmission is optically modulated within the picosecond and nanosecond time scale, respectively. This ultrafast dynamic behavior of all-optical modulation is attributed to defects introduced in the amorphous Ge, which operates as trap-assisted recombination sites for accelerating the relaxation of charge carriers. Equally important, the slow speed response and the broadened time window are defined by the integrated Si film, which make the device more tolerable to the uncertainty of delay time while preserving an ultrafast switching. Therefore, the EIT hybrid device with multiple photoactive materials has gone some way towards promoting the next-generation multifunctional THz components.

References

[1] Yoo S, Lee S, Park QH. Loss-free negative-index metamaterials using forward light scattering in dielectric meta-atoms. ACS Photonics 2018;5:1370–4.

[2] Shelby RA, Smith DR, Schultz S. Experimental verification of a negative index of refraction. Science 2001;292:77–9.

[3] Zhao XG, Wang Y, Schalch J, et al. Optically modulated ultra-broadband all-silicon metamaterial terahertz absorbers. ACS Photonics 2019;6:830–7.

[4] Schittny R, Kadic M, Buckmann T, Wegener M. Invisibility cloaking in a diffusive light scattering medium. Science 2014;345:427–9.

[5] Manjappa M, Pitchappa P, Wang N, Lee C, Singh R. Active control of resonant cloaking in a terahertz MEMS metamaterial. Adv Opt Mater 2018;6:1800141.

[6] Suen JY, Fan K, Padilla W. A zero-rank, maximum nullity perfect electromagnetic wave absorber. Adv Opt Mater 2019;7:1801632.

[7] Watts CM, Liu X, Padilla WJ. Metamaterial electromagnetic wave absorbers. Adv Mater 2012;24:OP98–OP120.

[8] Yang QL, Gu JQ, Xu YH, et al. Broadband and robust metalens with nonlinear phase profiles for efficient terahertz wave control. Adv Opt Mater 2017;5:1601084.

[9] Kim T-T, Kim H-D, Zhao R, et al. Electrically tunable slow light using graphene metamaterials. ACS Photonics 2018;5:1800–7.

[10] Wang Y, Leng Y, Wang L, et al. Broadband tunable electromagnetically induced transparency analogue metamaterials based on graphene in terahertz band. Appl Phys Express 2018;11:062001.

[11] Zhang S, Genov DA, Wang Y, Liu M, Zhang X. Plasmon-induced transparency in metamaterials. Phys Rev Lett 2008;101:047401.

[12] Chen J, Wang P, Chen C, Lu Y, Ming H, Zhan Q. Plasmonic EIT-like switching in bright-dark-bright plasmon resonators. Opt Express 2011;19:5970.

[13] Francescato Y, Giannini V, Maier SA. Plasmonic systems unveiled by Fano resonances. ACS Nano 2012;6:1830–8.

[14] Liu N, Langguth L, Weiss T, et al. Plasmonic analogue of electromagnetically induced transparency at the Drude damping limit. Nat Mater 2009;8:758–62.

[15] Cao W, Singh R, Zhang C, Han J, Tonouchi M, Zhang W. Plasmon-induced transparency in metamaterials: active near field coupling between bright superconducting and dark metallic mode resonators. Appl Phys Lett 2013;103:101106.

[16] Liu H, Ren G, Gao Y, Lian Y, Qi Y, Jian S. Tunable subwavelength terahertz plasmon-induced transparency in the InSb slot waveguide side-coupled with two stub resonators. Appl Opt 2015;54:3918.

[17] Limonov MF, Rybin MV, Poddubny AN, Kivshar YS. Fano resonances in photonics. Nat Photonics 2017;11:543–54.

[18] Huang Y, Li L, Lin Y-H, Nan C-W. Liquid exfoliation few-layer SnSe nanosheets with tunable band gap. J Phys Chem C 2017; 121:17530–7.

[19] Srivastava YK, Chaturvedi A, Manjappa M, et al. MoS$_2$ for ultrafast all-Optical switching and modulation of THz Fano metaphotonic devices. Adv Opt Mater 2017;5:1700762.

[20] Cai H, Huang Q, Hu X, et al. All-optical and ultrafast tuning of terahertz plasmonic metasurfaces. Adv Opt Mater 2018;6:1800143.

[21] Zhang C, Ouyang H, Miao R, et al. Anisotropic nonlinear optical properties of a SnSe flake and a novel perspective for the application of all-optical switching. Adv Opt Mater 2019;7:1900631.

[22] Polat EO, Kocabas C. Broadband optical modulators based on graphene supercapacitors. Nano Lett 2013;13:5851–7.

[23] Soavi G, Wang G, Rostami H, et al. Broadband electrically tunable third-harmonic generation in graphene. Nat Nanotechnol 2018;13:583–8.

[24] Zhong J, Peng Y, Li Y, Xing C. Solar-inspired water purification based on emerging 2D materials: status and challenges. Solar RRL 2020;201900400.

[25] Hu Y, Jiang T, Sun H, et al. Ultrafast frequency shift of electromagnetically induced transparency in terahertz metaphotonic devices. Laser Photonics Rev 2020;1900338.

[26] Wu L, Xie Z, Lu L, et al. Few-layer tin sulfide: a promising black-phosphorus-analogue 2D material with exceptionally large nonlinear optical response, high stability, and applications in all-optical switching and wavelength conversion. Adv Opt Mater 2018;6:1700985.

[27] Song Y, Shi X, Wu X, Tang D. Recent progress of study on optical solitons in fiber lasers. Appl Phys Rev 2019;6:021313.

[28] Zheng J, Tang X, Yang Z, et al. Few-layer phosphorene-decorated microfiber for all-optical thresholding and optical modulation. Adv Opt Mater 2017;5:1700026.

[29] Liang X, Ye X, Wang C, et al. Photothermal cancer immunotherapy by erythrocyte membrane-coated black phosphorus formulation. J Control Release 2019;296:150–61.

[30] Xing C, Huang W, Xie Z, et al. Ultra-small bismuth quantum dots: facile liquid-phase exfoliation, characterizations, and application in high-performance UV-vis photo-detector. ACS Photonics 2018;5:621–9.

[31] Hu Y, Jiang T, Zhou J, et al. Ultrafast terahertz frequency and phase tuning by all-optical molecularization of metasurfaces. Adv Opt Mater 2019;7:1970084.

[32] Manjappa M, Srivastava YK, Cong L, Al-Naib I, Singh R. Active photoswitching of sharp Fano resonances in THz metadevices. Adv Mater 2017;29:1603355.

[33] Shcherbakov MR, Liu S, Zubyuk VV, et al. Ultrafast modulation of femtosecond laser pulses in direct-gap semiconductor metasurfaces with magnetic resonances. Nat Commun 2017;8:17.

[34] Fan K, Zhao X, Zhang J, et al. Metamaterial-enhanced nonlinear responses in semiconductors as a THz detection platform. IEEE Trans Terahertz Sci Technol 2013;3:702.

[35] Shen NH, Massaouti M, Gokkavas M, et al. Optically implemented broadband blueshift switch in the terahertz regime. Phys Rev Lett 2011;106:037403.

[36] Fan K, Strikwerda AC, Zhang X, Averitt RD. Tuning the polarization state of light via time retardation with a microstructured surface. Phys Rev B 2013;87:161104.

[37] Hu Y, Jiang T, Zhou J, Hao H, Sun H. Ultrafast terahertz transmission/group delay switching in photoactive WSe$_2$-functionalized metaphotonic devices. Nano Energy 2020;68:104280.

[38] Manjappa M, Srivastava YK, Solanki A, Kumar A, Sum TC, Singh R. Hybrid lead halide perovskites for ultrasensitive photoactive switching in terahertz metamaterial devices. Adv Mater 2017;29:1605881.

[39] Cong LQ, Yogesh KS, Ankur S, Tze CS, Ranjan S. Perovskite as a platform for active flexible metaphotonic devices. ACS Photonics 2017;4:1595–601.

[40] Zhou J, Hu Y, Jiang T, Ouyang H, Li H, Sui Y. Ultrasensitive polarization-dependent terahertz modulation in hybrid perovskites plasmoninduced transparency devices. Photonics Res 2019;7:994.

[41] Zhang Y, Lim C, Dai Z, Yu G. Photonics and optoelectronics using nano-structured hybrid perovskite media and their optical cavities. Physics Rep 2019;795:1–51.

[42] Xie Z, Zhang F, Liang Z, et al. Revealing of the ultrafast third-order nonlinear optical response and enabled photonic application in two-dimensional tin sulphide. Photonics Res 2019;7:494.

[43] Xie Z, Xing C, Huang W, et al. Ultrathin 2D nonlayered tellurium nanosheets: facile liquid-phase exfoliation, characterization, and photoresponse with high performance and enhanced stability. Adv Fun Mater 2018;28:1705833.1–1705833.11.

[44] Xie Z, Chen S, Duo Y, et al. Biocompatible two-dimensional titanium nanosheets for multimodal imaging-guided cancer theranostics. ACS Appl Mater Interf 2019;11:22129–40.

[45] Xing C, Xie Z, Liang Z, et al. 2D nonlayered selenium nanosheets: facile synthesis, photoluminescence, and ultrafast Photonics. Adv Opt Mater 2017;5:1700884.

[46] Huang W, Xie Z, Fan T, et al. Black-phosphorus-analogue tin monosulfide: an emerging optoelectronic two-dimensional material for high-performance photodetection with improved stability under ambient/harsh conditions. J Mater Chem C 2018;6:9582–93.

[47] Fan T, Xie Z, Huang W, Li Z, Zhan H. Two-dimensional non-layered selenium nanoflakes: facile fabrications and applications for self-powered photo-detector. Nanotechnology 2019;30:114002.

[48] Xie Z, Wang D, Fan T, et al. Black phosphorus analogue Tin sulfide nanosheets: synthesis and application as near-infrared photothermal agents and drug delivery platforms for cancer therapy. J Mater Chem B 2018;10:1039. C8TB00729B.

[49] Yeh TT, Shirai H, Tu CM, et al. Ultrafast carrier dynamics in Ge by ultra-broadband mid-infrared probe spectroscopy. Sci Rep 2017;7:40492.

[50] Cooke DG, MacDonald AN, Hryciw A, et al. Transient terahertz conductivity in photoexcited silicon nanocrystal films. Phys Rev B 2006;73:193311.

[51] Chen HT, Padilla WJ, Zide JM, et al. Ultrafast optical switching of terahertz metamaterials fabricated on ErAs/GaAs nanoisland superlattices. Opt Lett 2007;32:1620.

[52] Lim WX, Manjappa M, Srivastava YK, et al. Ultrafast all-Optical switching of germanium-based flexible metaphotonic devices. Adv Mater 2018;30:1705331.

[53] Yahiaoui R, Burrow JA, Mekonen SM, et al. Electromagnetically induced transparency control in terahertz metasurfaces based on bright-bright mode coupling. Phys Rev B 2018;97:155403.

[54] Xu Q, Su X, Ouyang C, et al. Frequency-agile electromagnetically induced transparency analogue in terahertz metamaterials. Opt Lett 2016;41:4562.

[55] Liu Y, Fang N, Wu D, Sun C, Zhang X. Symmetric and antisymmetric modes of electromagnetic resonators. Appl Phys A 2007;87:171–4.

[56] Kamaraju N, Rubano A, Jian L, et al. Subcycle control of terahertz waveform polarization using all-optically induced transient metamaterials. Light Sci Appl 2014;3:e155.

[57] Strait JH, George PA, Levendorf M, Blood-Forsythe M, Rana F, Park J. Measurements of the carrier dynamics and terahertz response of oriented germanium nanowires using optical-pump terahertz-probe spectroscopy. Nano Lett 2009;9:2967–72.

[58] Green MA. Self-consistent optical parameters of intrinsic silicon at 300 K including temperature coefficients. Solar Energy Mater Solar Cells 2008;92:1305–10.